Two New Ejecta-Dominated Galactic Supernova Remnants: G337.2−0.7 and G309.2−0.6

Cara E. Rakowski[1,2], John P. Hughes[1,2],
and
Patrick Slane[3]

ABSTRACT

We present the analysis of new X-ray observations of two Galactic radio supernova remnants (SNRs), G337.2−0.7 and G309.2−0.6. Both remnants exhibit line-rich thermal spectra that require highly non-solar elemental abundance ratios. In each case, Si and S are unequivocally overabundant compared to solar based purely on the measured equivalent width of the Kα line complex. Detailed nonequilibrium ionization spectral analysis of these remnants, using a single temperature, single ionization age model, confirm the overabundances, yielding Si, S and Ar abundances many times their solar values: 3 to 5 times solar for G337.2−0.7 and greater than 3 to 10 times solar for G309.2−0.6. We also find that for both remnants, Ne and Mg are underabundant relative to Si, and for G309.2−0.6, Ca and Fe as well are relatively underabundant. This is the first detection of metal-rich, non-solar abundance material in these remnants, identifying them as young ejecta-dominated SNRs. Further support for their youth comes from the distances that we estimate from the fitted column densities (less than 15 kpc for G337.2−0.7, and 4 ± 2 kpc for G309.2−0.6). From the implied sizes of the remnants at these distances we infer relatively young ages (2000 to 4500 years for G337.2−0.7, and 700 to 4000 years for G309.2−0.6). Finally we note that no compact object has yet been found within G337.2−0.7, but an X-ray point source is evident within the radio shell of G309.2−0.6, although its nature remains unknown.

Subject headings: Supernova remnants – X-rays: general – ISM: abundances

1. Introduction

Supernovae (SNe) are the birthplace of almost all metals that exist in the universe. Models of the explosive nucleosynthesis that occurs in SNe are used to study the evolution of the interstellar medium, external galaxies, and even clusters of galaxies. Young supernova remnants (SNRs), whose emission is still dominated by the ejecta, are the best test for our models of nucleosynthesis. However, these models have primarily been tested in the ensemble, against the abundances of large regions, such as the solar neighborhood, where those abundances are assumed to be the product of many representative supernovae. Direct measurements of the nucleosynthetic yields of individual supernova, using the abundances found in their ejecta, has been much more limited. Cas A, which has been extensively studied across the wavebands (e.g., Chevalier & Kirshner 1979; Fesen, Becker, & Blair 1987; Douvion, Lagage, & Cesarsky 2000; Hughes et al. 2000) is more the exception than the rule.

Considering that the Galactic SNe rate is widely believed to be a few per century, there should have been on the order of 5–10 Galactic SNe since the last historical one observed by Kepler in 1604. Additionally there must be a sizeable population of SNRs less than ∼2000 years old or

[1]Department of Physics and Astronomy, Rutgers The State University of New Jersey, 136 Frelinghuysen Road, Piscataway NJ 08854-8019; E-mail: rakowski@physics.rutgers.edu and jph@physics.rutgers.edu

[2]Also Service d'Astrophysique, L'Orme des Merisiers, CEA-Saclay, 91191 Gif-sur-Yvette Cedex France

[3]Harvard-Smithsonian Center for Astrophysics, 60 Garden Street, Cambridge MA 02138

so. However, prior to *ASCA* there were only a handful of young remnants known and they fell into two classes: the remnants of young historical SNe (e.g. Tycho, Kepler) and oxygen-rich SNRs (e.g. Cas A, G292.0+1.8) classified based on their optical characteristics. Studies with the *Advanced Satellite for Cosmology and Astrophysics* (*ASCA*) have added a third class of presumably young remnants: those for which optical evidence of ejecta is absent, but whose X-ray spectra show enhanced, non-solar abundances, and hence are likely to be ejecta-dominated (e.g. W49B in the Galaxy, Fujimoto et al. 1995; or N103B in the LMC, Hughes et al. 1995). Clearly, identifying and studying new X-ray ejecta-dominated SNRs will be vital for understanding the SNR population and the process of nucleosynthesis.

G337.2−0.7 and G309.2−0.6 are part of our ongoing project surveying small Galactic supernova remnants in an attempt to identify more ejecta-dominated SNRs through their X-ray emission. G337.2−0.7 and G309.2−0.6 were first identified as SNR candidates based on their possible non-thermal radio emission (Green 1974). These identifications were confirmed in the radio in the MOST supernova remnant catalogue (Whiteoak & Green 1996). G309.2−0.6 was the subject of a detailed radio study by Gaensler, Green, & Manchester (1998) (hereafter GGM) using the Australia Telescope Compact Array (ATCA). The radio images of G337.2−0.7 and G309.2−0.6 are given in Figures 1a and 2a. G337.2−0.7 shows a barely resolved, possibly shell-like morphology, with a diameter of ∼6 arcminutes and an overall radio surface brightness at 843 MHz of 11×10^{-21} W m^{-2} Hz^{-1} sr^{-1} (Whiteoak & Green 1996). G309.2−0.6 exhibits a more complex morphology in the radio with evidence for 2 shells, diameters 12 and 15 arcminutes, and a possible jet-like feature to the northeast (GGM) which appears as a faint wisp in our reproduction. The SNR has a surface brightness at 843 MHz of 5.4×10^{-21} W m^{-2} Hz^{-1} sr^{-1} (Whiteoak & Green 1996). GGM find a distance for G309.2−0.6 of between 5.4±1.6 and 14.1±0.7 kpc using HI absorption measurements. GGM's lower limit was found based on absorption towards the SNR, and the upper limit was constrained by the lack of a positive velocity absorption feature which was present in other nearby sources, indicating that the remnant must be closer than those sources.

These SNRs are positionally coincident with bright sources from the *ROSAT* All-Sky Survey (RASS) (Voges et al. 1999). G337.2−0.7 corresponds to source 1RXS J163931.4−475019, with a count rate of 0.05 ± 0.02 counts s^{-1}, and G309.2−0.6 is close to source 1RXS J134651.1−624843 with a count rate of 0.06 ± 0.02 counts s^{-1}. These measurements indicated the presence of soft X-ray emission from these remnants; our *ASCA* observations were required to determine the nature of this emission.

The *ASCA* X-ray observations of these remnants provide new insight into their physical properties. The *ASCA* band (0.7−10 keV) spans emission lines of Ne, Mg, Si, S, Ar, Ca, and Fe, allowing for examination of the abundances, temperature, density and ionization state in the X-ray emitting region, as well as the line-of-sight absorbing column density, although individual emission lines are, in general, not resolved by *ASCA*. This first examination of the X-ray spectra from these remnants reveals line-rich thermal emission with strong indications of highly non-solar elemental abundance ratios.

In section 2 we outline the data reduction, background subtraction and general image analysis. In section 3 we present the spectroscopy and nonequilibrium ionization (NEI) analysis, along with the resulting abundances. Section 4 discusses the distances, ages, and nucleosynthesis models. Finally, we summarize our results and highlight areas for further investigation in section 5.

2. Data Reduction and Image Analysis

The primary X-ray observations used in this work were taken with instruments aboard *ASCA*, which has two Solid State Imaging Spectrometers (SIS 0 and SIS 1) which each consist of four CCD chips, and two Gas Imaging Spectrometers (GIS 2 and GIS 3) (For details concerning the *ASCA* satellite see Tanaka, Inoue & Holt, 1994). Our observations were taken in 1997 March for G337.2−0.7 and 1999 April for G309.2−0.6, both late in the life of *ASCA*, after significant cosmic-ray induced degradation of the CCDs had occurred. Two CCD mode was chosen to minimize the effect of residual dark current due to radiation damage (the amount of dark current increases

with the readout time which scales with the number of chips), while still covering the full extent of each remnant.

The GIS and SIS data were screened with the standard *ASCA* criteria.[4] Both light-leak and contamination from cosmic rays are a concern. For the GIS data, rise-time information was used to reject non X-ray events. To determine if the standard screening were sufficient for our SIS data, we checked to see if there were any significant differences in the spectra for medium versus high bit-rate, night versus day, different cutoff rigidities, bright versus faint mode, and between the two SIS instruments for each source studied. Since we found no significant secular changes in the spectra, we concluded that indeed the standard screening was reasonable. After screening, the exposure times for G337.2−0.7 were ∼14.6 ksec in each of the SIS instruments (bright and faint modes combined, both medium and high bit-rate). Likewise the good exposure times for G309.2−0.6 were ∼15.4 ksec with SIS 0, but only ∼4.6 ksec with SIS 1.

Both the GIS and SIS data were used in the image analysis. Due to its higher temporal resolution (∼0.016 s) only the high-bit-rate GIS data were used for timing analysis. For the spectral analysis we chose to focus on the higher resolution SIS data. The GIS spectra are qualitatively similar, but detailed spectral analysis of these data is more difficult because, at the time of this work, significant uncertainties exist in the GIS gain (as much as 45 eV shifts near the Si Kα line complex; Ken Ebisawa, personal communication). For an emission-line dominated spectrum, such as the ones here, this uncertainty would strongly influence our results, and hence we choose to use only the SIS spectra.

2.1. G337.2−0.7, image analysis and background subtraction

Images of G337.2−0.7 in various wavebands are shown in Figure 1. In Figure 1a, we compare the MOST radio image with contours from the overall (0.7-10.0 keV) *ASCA* SIS X-ray band. We also present the *ASCA* SIS X-ray image separated into "soft" (Figure 1c) and "hard" (Figure 1d) bands, where the soft band (0.7−1.5 keV) covers L-shell lines of Fe and Ca, and K-shell lines of Ne and Mg, and the hard band (1.5−10.8 keV) includes emission from the K-shell lines of Si, S, Ar, Ca and Fe. Both bands include continuum emission. These images were made by combining the SIS 0 and SIS 1 images in those energy bands, correcting for the exposure time in any given pixel and smoothing the image by convolving it with a gaussian of $\sigma \sim 0.8'$. In the X-ray band G337.2−0.7 appears as a featureless source ∼6′ in diameter, comparable to the MOST radio image, and therefore nearly unresolved by *ASCA*. There is no significant change in the size of the remnant with energy, especially at high energies, hence there is no evidence for the presence of a hard, pulsar-powered, synchrotron nebula within the remnant. We do not show the GIS images since they do not reveal any new information beyond that shown by the SIS.

The soft band image (Figure 1c) shows another source toward the northeast of the SNR, which we designate AX J16398−4746. Figure 1b overlays the soft band contours on the Digitized Sky Survey (DSS) image from the UK Schmidt Telescope plates. There is a bright star (HD 149901, spectral class F5, $m_V = 7.4$) that is positionally coincident with the soft X-ray source. This source has an X-ray count rate of $(5.0 \pm 0.6) \times 10^{-3}$ counts s^{-1} in a circular region of radius 1.7′, yielding a greater than 6σ detection of the source. The X-ray flux is $f_x \sim 5 \times 10^{-13}$ergs cm^{-2} s^{-1} (over the 0.3 to 3.5 keV band). The X-ray to optical flux ratio of $\log(f_x/f_v) \sim 4$ is consistent with that of an F5 star according to Maccacaro et al. (1988) making plausible the identification of HD 149901 as the X-ray source.

The spectrum for G337.2−0.7 was extracted from a circular region with radius 3.7′ which excluded the soft emission from the HD star, but was sufficiently large to account for the point spread function (PSF) of the *ASCA* SIS and the extent of the source. The spectra from the two SIS instruments were combined and then grouped into bins containing at least 25 counts each so that the χ^2 statistic could be used in fitting the spectrum. We followed the standard *ASCA* prescription for generating a response function for com-

[4] Interested readers are referred to the *ASCA* Guest Observer Facility, and the *ASCA* Data Reduction Guide at http://heasarc.gsfc.nasa.gov/docs/asca/abc/abc.html for more details.

bined SIS data. Routine background subtraction of the average cosmic and detector background was also done using publically available high Galactic latitude fields. For the SNR we find a count rate of 0.099 ± 0.002 SIS counts s^{-1}, where only the high Galactic latitude background (with rate 0.018 SIS counts s^{-1}) has been subtracted.

For G337.2−0.7, additional background X-ray emission from the Galactic ridge was found to be present. To model this emission, a source-free control region of the same size as the SNR region was extracted from elsewhere within the SIS field of view. Using an absorbed powerlaw model, which was a good fit to the data, with best-fit column density $N_{\rm H} \sim 3.9 \times 10^{21}$ atoms cm^{-2} and spectral index, $\alpha_p \sim 1.3$, we find a surface brightness of 3×10^{-7} ergs s^{-1} cm^{-2} sr^{-1} in the 0.5-10 keV band. This is consistent with the surface brightness of Galactic ridge emission found near G328.4+0.2 by Hughes, Slane, & Plucinsky (2000), and the Galactic ridge emission found with the *GINGA* satellite by Yamauchi (1991). This absorbed powerlaw model for our control region was then included as an additional component in the spectral fits for the SNR, in order to account for the Galactic ridge emission contained in the SNR spectrum. Our model implies a count rate of 0.016 SIS counts s^{-1} from the Galactic ridge in the SNR region.

2.2. G309.2−0.6

In Figure 2 we show images of G309.2−0.6 in various wavebands. Figure 2a shows the *ATCA* 1.3 GHz image with broad-band X-ray contours of the *ASCA* GIS observations that were exposure corrected, summed and smoothed with a $\sigma = 1'$ gaussian. The field of view of the GIS extends slightly beyond that shown in Figure 2a; however no significant X-ray emission was detected beyond that shown. In particular the region of the radio jet toward the north is not detected.

For the *ASCA* SIS X-ray images of G309.2−0.6, we separated the emission into the band in which extended emission was significant (1.0-3.2 keV, Figure 2d), and energies at which an unresolved source in the field of view, 1WGA J1346.5−6255, dominates the emission (0.7-1.0 keV and 3.2-10.0 keV, Figure 2c). These images were exposure corrected, combined and smoothed with a $\sigma = 0.8'$ gaussian. Both the SNR (0.14 SIS counts s^{-1}, see below) and the unresolved source (0.027 ± 0.001 SIS counts s^{-1} in a $\sim 1'$ region) are detected at much greater than the 6σ level. As we will show in section 3.2, it appears that effectively all of the emission in the 0.7-1.0 keV and 3.2-10.0 keV bands comes from the unresolved source.

In Figure 2b, we show the *ROSAT* PSPC X-ray contours overlayed on the DSS greyscale image of this region. For all instruments the position of the unresolved source is consistent with the optical cluster NGC 5281 as shown in Figure 2b and previously noted for the *ROSAT* data by GGM. Modeling the spectrum of the point source with an absorbed powerlaw, column density $N_{\rm H} = 2.6^{+1.8}_{-1.4} \times 10^{21}$ atoms cm^{-2}, and spectral index $\alpha_p = 1.5 \pm 0.3$, we find that the flux from this source in the 0.3−3.5 keV band is $\sim 1.3 \times 10^{-12}$ ergs cm^{-2} s^{-1}. This flux is consistent with that expected from HD 119682, the third brightest star in NGC 5281, an O9, $m_V = 7.89$ star, using the relation of Maccacaro et al. (1988), although it is on the X-ray bright side of the distribution for such a stellar type. In Figure 2b this star is the brightest one within the highest *ROSAT* contour. It is also possible that the point source is a compact object orbiting one of the stars in the cluster NGC 5281.

There is even a more intriguing possibility, that the point source is related to the SNR itself. Given that the absorbing column density found is similar to that towards the remnant (see section 3.2 and Table 2), it is reasonable to expect the point source to be at the same distance as the remnant. The photon index of the point source is broadly consistent with a pulsar or synchrotron nebula interpretation. To search for pulsations from this source we chose a region $1'$ in radius in the GIS data to maximize the signal to noise, yielding 177 counts total in the two GIS instruments, with as much as 20% contamination from the SNR and cosmic x-ray background. No significant peak was found in the Fourier transform of the GIS lightcurve in the 2×10^{-3} Hz to 32 Hz frequency range. The lightcurve was epoch folded over periods near each of the largest peaks in the Fourier transform, but no pulsations were found above even the 1 σ confidence limit. However, due to the small number of counts, this only limits the pulse fraction to be less than ∼85% over this frequency range at the 99.99% confidence level (see Leahy et al. 1983).

Due to the broad PSF of *ASCA* the emission from the unresolved source spreads over the field of view and significantly contaminates the remnant emission. As a consequence, the spectral analysis of G309.2−0.6 requires special careful treatment.

For G309.2−0.6, spectra from two source regions were extracted, one circular region of radius $0.95'$ which contained the most obvious emission from the point source, and another which excluded this region, and contained the full extent of the remnant as seen in the 1.0-3.2 keV band, with a radius of $5.6'$. The spectra and response functions from the two SIS instruments were combined in the same manner as for G337.2−0.7, and routine background subtraction was done using the high Galactic latitude background files.

For G309.2−0.6, we also extracted control regions to model the Galactic ridge background, but we found only one region with significant counts after subtracting the cosmic background and this region's emission could easily be attributed to instrumental scattering from the supernova remnant and the point source. Therefore no additional Galactic ridge background was subtracted for G309.2−0.6.

The primary source of contamination to the *ASCA* SIS spectrum of G309.2−0.6 comes from the point source. To model how the PSF of *ASCA* behaves at this particular position on the chip as a function of energy, we chose to investigate archival data of an isolated point source observed at a similar position on the chip in the same observational configuration as our data. The cataclysmic variable source, SS Cyg (*ASCA* seq. no. 30001000), was found to be a reasonable match, most notably in the respect that the source is the same distance from the chip gap. This source is also bright, so there are sufficient counts to use it to model the PSF.

Using regions nominally identical in size and position to those of the G309.2−0.6 point source and remnant regions, we found the ratio of counts in the inner smaller region to the outer region for each energy bin. We then used this ratio to model the contamination from the G309.2−0.6 point source into the SNR region. The contamination spectrum was modeled with an absorbed powerlaw and this powerlaw was used as one of the components for the model of the SNR emission. It should be noted that the ratio was not strongly dependent on photon energy, and that merely renormalizing the original point source powerlaw model by an appropriate amount gave a reasonable fit for the modeled SNR contamination spectrum.

Various sources of systematic error in the model of the point source contamination were investigated, that could either increase (+) or reduce (−) the contamination from the point source into the SNR region. These were as follows: (1) small changes in the positions of the extraction regions for the point source (±6%) and the SNR (+6%) based on the SS Cyg data, (2) contamination of the point source by SNR emission that falls in the point source region (−2% to −10%)), and (3) including a Galactic ridge background component (+14%). To account for these possible sources of error, we have investigated both the nominal model for the contamination discussed above as well as a model in which the contaminating flux has been decreased by 10%. However, we can safely ignore a model with the contaminating flux increased by even as little as a few percent since this would overpredict the emission from the remnant region below 1 keV and above 3.2 keV.

3. Spectral Analysis

We modeled the emission from each remnant with a nonequilibrium ionization (NEI) model. The NEI model used in this analysis is the single-temperature, single-timescale model from Hughes & Singh (1994) which assumes that the SNR emission can be described by an average temperature kT and ionization timescale $n_e t$, which parameterizes the departure from ionization equilibrium. The elements included in this study are H, He, C, N, O, Ne, Mg, Si, S, Ar, Ca, and Fe whose baseline solar abundances are as given by Raymond & Smith (1977): 12.0, 10.93, 8.52, 7.96, 8.82, 7.92, 7.42, 7.52, 7.2, 6.9, 6.3, 7.6 dex respectively. We note that the inferred abundances are model dependent, however the basic conclusions should remain unchanged.

We explored models with three different sets of elemental abundances in our NEI spectral fits. First, the abundances of all the elements were fixed at their solar values to determine a baseline model fit. Next, the overall metallicity was allowed to vary freely, i.e. the H and He abundances were fixed at their solar values, and the abun-

dances of all higher Z elements were allowed to vary, but with abundances fixed relative to one another. In our final model, which we refer to as the varying abundances model, C, N, and O were fixed to their solar abundances, Ne and Mg were varied together, while Si, S, Ar, Ca and Fe were each individually allowed to vary freely. The rationale behind this prescription is the following: the emission lines of C, N, and O are below or at the lower limits of the detected energy range so that they have little or no effect on the results. The emission lines from Ne and Mg, although detectable, are highly absorbed so they are weak and independent determination of each abundance separately is not well constrained. For G337.2−0.7 the observed ratio of Ne to Mg was similar to the solar ratio when both were allowed to be free, but neither was tightly constrained in this method, so we tied their abundances together. For G309.2−0.6 the abundance of Ne was not individually constrained in any way, so it could have been set to solar abundance. However, since the preferred ratio of Ne to Mg abundance was close to solar, for G309.2−0.6, we chose to link the Ne abundance to the Mg abundance as was done for G337.2−0.7. Si, S, Ar, Ca, and Fe abundances were allowed to vary freely because they have detectable emission lines in the *ASCA* SIS X-ray band, even for a highly absorbed source.

3.1. G337.2−0.7

Figure 3 shows the combined SIS spectra from G337.2−0.7 with the best-fit spectral model (see below). The most obvious features of this spectrum are the emission lines of Si, S and Ar, as indicated on figure 3. The lines themselves are each an amalgam of multiple emission lines of different ionic species, whose individual lines are not resolved at this spectral resolution. Due to degradation of the CCD He-like and H-like lines are no longer resolvable from each other. For instance, the feature around 1.9 keV contains Kα (n = 2 $\rightarrow$ n = 1) lines predominantly of He-like and H-like Si. This line blend is quite strong. Using a simple bremsstrahlung continuum and three gaussian lines with an absorbing column we find that the equivalent widths (EWs) for the Si, S and Ar Kα line complexes of G337.2−0.7 are about 660, 570, and 320 eV, respectively ($\pm$50 eV at 1σ). In comparison, the maximum equivalent widths for a solar abundance plasma, $\mathrm{EW}_{\mathrm{max},\odot}$, for Si, S, and Ar for temperatures between 0.4 and 5.0 keV, any ionization timescale, and any absorbing column density are 550, 350, 400 eV respectively. From this we can immediately see that Si and S are significantly enhanced in G337.2−0.7. Additionally, the temperatures, timescales and column densities at which the $\mathrm{EW}_{\mathrm{max},\odot}$ are found are not consistent with the data. For example the modeled energies of the lines are different from those in the gaussian line fits indicating that the modeled ionization state is not correct and the line ratios between the different atomic species are dissimilar from those found in G337.2−0.7.

For G337.2−0.7, the various spectral models yield the following. With all the abundances fixed to their solar values the best-fit χ^2 is 170.5 (73 degrees of freedom), clearly not a good fit. The model with a single variable metallicity prefers an extremely large metallicity (7 times solar) and does slightly better at fitting the spectra than the solar abundance model with a χ^2 of 155.7 (72 degrees of freedom). Both these models have $kT \sim 0.7$ keV, $n_e t \sim 5\times10^4$ cm^{-3} yr, and $N_{\mathrm{H}} \sim 4\times10^{22}$ atoms cm^{-2}. With similar temperature, timescale and absorbing column density (see Table 1), the varying abundances model provides a much improved description of the spectrum. It yields a best-fit χ^2 of 103.1 (67 degrees of freedom). This reduction in χ^2 implies a F_χ-stat confidence level for the addition of six new parameters (compared to the solar model) of 99.5%. Si, S and Ar are all significantly overabundant compared to their solar values confirming what we found above from the line equivalent widths, whereas the best-fit abundance of Ne and Mg is zero.

Using the varying abundances model, we mapped the allowed region of parameter space for temperature and ionization timescale. As given in Table 1, the 1σ range of kT and $n_e t$ is $kT = 0.82-0.89$ keV and $n_e t = (2.1-8.0)\times10^4$ cm^{-3} yr. Note that the upper limit on $n_e t$ is simply the value at which the equilibrium ionization fractions are attained. We see that a low temperature and near equilibrium ionization fractions are preferred. The H density, corresponding to the best-fit emission integral is $1.4\pm0.3 D_{10\mathrm{kpc}}^{-1/2}$ atoms cm^{-3} scaled to a nominal distance of 10 kpc (see section 4). The absorbing column density is high, $(3.5\pm0.3)\times10^{22}$ atoms cm^{-2}.

In figure 4 we present a concise summary of the spectral fit results, including the variation with temperature of the best-fit χ^2, the ionization timescale, the best-fit abundance of Si (relative to solar), and the abundances of the other elements relative to Si. The range plotted corresponds to the 3σ allowed range on kT. In figure 5 we present the best fit values and 1σ limits on the relative metal abundances in the form, $(\mathrm{Z/Si})\times[(\mathrm{Si/H})_\odot/(\mathrm{Z/H})_\odot]$.

According to figures 4 and 5, Si, S, Ar, and Fe are all constrained at the 1σ level to be greater than 1.7 times their solar abundances, and Si is constrained to be at least 3.2 times its solar abundance. Furthermore, the overabundance of Si, S, Ar and Ca hold true throughout the entire allowed 3σ range on kT. In addition to these enhanced abundances, further evidence for the unusual nature of the emission comes from the non-solar ratio of Ne and Mg to Si. Although the absolute abundances of Ne and Mg are allowed to be greater than solar, the ratio of their abundance to Si is constrained to be less than 0.2 times the solar ratio at 1σ. Unfortunately the situation is not so clear for the Fe abundance, since, in addition to the best-fit abundance of Fe (which is super-solar), there is a region of parameter space for which its abundance is zero.

3.2. G309.2−0.6

Figure 6 shows the combined SIS spectra of G309.2−0.6 with the best-fit spectral model. This spectrum exhibits very strong emission lines from Si, S and Ar. As before, using a simple bremsstrahlung continuum and three gaussian lines with an absorbing column we find EWs for Si, S, and Ar of 1160 ± 100 eV, 1280 ± 100 eV, and 510 ± 200 eV, respectively, for the nominal contamination model (to repeat, $\mathrm{EW}_{\mathrm{max},\odot}$: 550, 350, and 400 eV for Si, S, and Ar). Furthermore, even if contamination from the point source is ignored entirely, the EWs of Si and S are 640 ± 50 eV and 550 ± 50 eV, still greater than the $\mathrm{EW}_{\mathrm{max},\odot}$ values.

G309.2−0.6 also requires non-solar relative abundances. Models with solar abundances or a single variable metallicity do not provide a good fit to the spectrum, for either point-source contamination model (i.e. nominal or one with 10% less contamination). In the case with nominal contamination, the best-fit solar abundance model and single variable metallicity model have χ^2 (d.o.f.) values of 111.0 (59) and 100.4 (58) respectively with $kT \sim 0.5$ keV, $n_e t \sim 6 \times 10^3$ cm^{-3} yr, and $N_{\mathrm{H}} \sim 5 \times 10^{22}$ atoms cm^{-2}. This should be compared to a χ^2 of 49.4 (53) for the varying abundance model (see Table 2). This large reduction in χ^2 corresponds to an F_χ-stat confidence level for the addition of these six new parameters (compared to the solar abundance model) of 99.5%.

Our spectral fits for G309.2−0.6 require extremely enhanced abundances. The best-fit value for the single variable metallicity is effectively infinite (>1000): in other words, the minimum χ^2 is found when emission from H and He becomes negligible. Similarly, high values are also found for the varying abundances model (see Table 2). At a minimum, Ne, Mg, Si, S and Ar are highly over-abundant, with lower limits of 2.0, 2.0, 10.9, 11.9 and 2.9 respectively (where this lower limit derives from the 1σ errors on the model with 10% less contamination than the nominal case). In fact a pure-metal plasma, composed of only those elements with obvious emission lines in this band is easily allowed within the 1σ limits of either contamination model. The relative elemental abundances quoted in Table 2 are also highly non-solar. In particular, the abundances of Ne, Mg, Ca and Fe relative to Si are all less than half the solar ratios.

For G309.2−0.6, where a pure metal plasma of just Ne, Mg, Si, S, Ar, Ca and Fe is allowed, it is apparent that the relevant abundance parameters to study are the abundance ratios to Si, not to H. In Figure 7, we plot χ^2, the ionization timescale, and the abundance ratios with Si as a function of kT over a wide range, for both contamination models. We note that throughout this range in kT the Si abundance is greater than 34 and 11.9 at the 1σ level for the nominal and 10% less contamination models respectively and moreover, must be greater than 6.5 and 3.9 respectively at the 99% confidence level. The pattern of variations here is similar to that for G337.2−0.7: Fe is only allowed for low temperatures, where Ne and Mg are at a local minimum, and the other relative abundances remain fairly constant throughout the range of parameter space. Si, S, Ar, Ne and Mg are all highly overabundant compared to solar over the entire

range of kT. In Figure 8 we present the best fit values and 1σ limits on the relative metal abundances in the form, $(\mathrm{Z/Si})\times[(\mathrm{Si/H})_\odot/(\mathrm{Z/H})_\odot]$, for both the nominal and the 10%-less contamination model. This figure also illustrates the dominance of Si and S emission and relative underabundance of Ne, Mg, Ar, Ca, and Fe.

The effect of the point source contamination on the derived abundances is important to note. As one might expect, since less of the continuum emission has been accounted for, the 10%-less contamination model yields lower abundances relative to H than the nominal contamination model does. However the abundances relative to Si are somewhat higher. Yet, the pattern of the relative abundances remains qualitatively the same, and the enhanced abundances persist even without any contamination model. We note that the 10%-less contamination model does a marginally better job of fitting the data (χ^2 of 48.6 vs. 49.4) but the difference in χ^2 is not significant.

Verification of our model for the point-source contamination of G309.2−0.6 comes from examining the *ROSAT* data on this remnant. The PSF of *ROSAT* is much finer than *ASCA* and hence we expect very little contamination of the SNR emission from the point source. After background subtraction, the *ROSAT* spectrum for the remnant shows very little emission below 1 keV (count rate = 0.01±0.004 counts s^{-1}, between 0.5−1.0 keV compared to 0.07±0.006 counts s^{-1} for 0.5−2.0 keV), which agrees with our model that point source contamination is causing effectively all the emission below 1 keV for the *ASCA* data. Modeling the *ROSAT* SNR emission with the best-fit model for just the SNR emission in *ASCA*, gives a slightly better χ^2 than a model assuming that what we define as contamination from the point source is actually SNR emission. Unfortunately, the χ^2 difference is not great enough to allow us to discriminate between these two cases. However we can conclude that our point source contamination models are fully consistent with the *ROSAT* data.

The dynamical parameters for G309.2−0.6 are less well constrained than for G337.2-0.7, because of the complication of the contaminating point source. Nevertheless the best-fit values of kT, $n_e t$, and N_H are all quite reasonable. G309.2−0.6 appears to have a somewhat higher temperature than G337.2-0.7 (1-2 keV vs. 0.8-0.9 keV). The ionization timescales for the two SNRs are consistent with each other and the 1σ ranges allow for equilibrium ionization for both remnants. G309.2−0.6 has a low absorbing column density, $\mathrm{N_H}$, $(0.3-1.0)\times10^{22}$ atoms cm^{-2}, similar to that found for the unresolved source, indicating that they are at approximately the same distance. The number density of hydrogen atoms, corresponding to the best-fit emission integral and a nominal distance of 5.4 kpc is very low, $n_\mathrm{H}=0.02^{+0.03}_{-0.01}D^{-1/2}_{5.4kpc}$ atoms cm^{-3}, reflecting the fact that hydrogen is not the dominant element in the X-ray emitting plasma as it would be under usual solar abundance conditions.

4. Discussion

Given the absorbing hydrogen column density measured from our X-ray spectra, it is possible to estimate the distances to G309.2−0.6 and G337.2−0.7. Following Chen et al. (1999), given a hydrogen column density, N_H, the relation between column density and optical color excess, $N_H = 5.9\times10^{21}\langle E_{B-V}\rangle$ (Predehl & Schmitt 1995) and the extinction per unit distance, $\langle E_{B-V}\rangle/d$, in the direction of a remnant one can estimate the distance to that remnant. For the extinction per unit distance, we use the contour diagrams of Lucke (1978). Since these measurements were for stars within 2 kpc of the sun, and the density of absorbing material is undoubtedly greater near the Galactic center, any distance estimates greater than 2 kpc in the direction towards the Galactic center should be viewed as upper limits.

For G309.2−0.6, with $N_\mathrm{H} = (0.7\pm0.3)\times10^{22}$, $\langle E_{B-V}\rangle/d \sim 0.3$ mag kpc^{-1}, we find $d \leq 4\pm2$ kpc. The distance thus found for G309.2−0.6, is consistent with the lower range of distances found by GGM, 5.4±1.6 kpc, which was found from H I absorption toward the remnant itself. This distance is consistent with that of the H II region, RCW80 lying $\sim 20'$ north of G309.2−0.6, as well as the location of the Scutum-Crux spiral arm of the Galaxy. Furthermore, for a distance of 5.4 kpc, GGM estimate an age of less than 4000 years and size of ∼9.5 pc in radius which is more consistent with its ejecta-dominated nature than a larger distance would be.

For the point source in G309.2−0.6, 1WGA

J1346.5−6255, which has $N_{\rm H} = 2.6^{+1.8}_{-1.4} \times 10^{21}$ atoms cm^{-2} we find $d = 1.5 \pm 1$ kpc, broadly consistent with the X-ray estimated distance to the SNR, but also consistent with the distance to the cluster NGC 5281 (1.3 kpc, Moffat & Vogt 1973).

The $N_{\rm H} = (3.5 \pm 0.3) \times 10^{22}$ atoms cm^{-2} and $\langle E_{B-V} \rangle / d \sim 0.4$ mag kpc^{-1} of G337.2−0.7 yield a distance upper limit of 15.5±1.5 kpc. This is much further than the applicability of the extinction per unit distance estimate, but is useful as an upper limit. In the direction of G337.2−0.7 the measured total column density is rather high, $\sim 5 \times 10^{22}$ atoms cm^{-2}; much of this material is likely to be distributed in molecular clouds and other dense regions in the Perseus, Scutum-Crux and Norma spiral arms and the 5 kpc molecular ring. Since a single large molecular cloud along the line of sight could be sufficient to account for all the X-ray absorption we see (e.g., Corbel et al. 1999), we can, at this time, only surmise that G337.2−0.7 is somewhere between the near and far sides of the Norma spiral arm at ∼5 kpc and ∼15 kpc. Measurements of the intensities and velocities of CO emission towards this remnant would allow us to determine the distribution of material along the line-of-sight. Combined with the X-ray column density, we could then estimate the remnant's distance, as has been recently done by Corbel et al. (1999) for SNR G337.0−0.1. In addition, radio measurements of H I absorption to G337.2−0.7 should be pursued as another constraint on its distance. For purposes of estimation in this work, we use a nominal distance of 10 kpc.

Given our distance estimates, we can place rough limits on the ages of the remnants. By assuming free-expansion at some typical velocity (5000 km s^{-1}) we can place a lower limit on the time since the explosion. For G337.2−0.7, distances of 10 and 15 kpc yield a lower limit of between 1700 and 2600 years. For G309.2−0.6 a distance of 4±2 kpc corresponds to a lower limit on the age of between 700 and 2000 years. Since our abundances indicate that these remnants are not yet in the Sedov phase, a nominal Sedov solution provides upper limits on the ages (see for instance Hamilton, Sarazin, & Chevalier 1983; Hughes, Hayashi, & Koyama 1998). This is because a Sedov solution would imply that the outer shock has been decelerated by the ambient medium more than we would expect for a remnant still dominated by emission from ejecta. For both remnants we assume an ambient density, $n_0 = 0.2$ cm^{-3}, and explosion energy, $E_0 = 10^{51}$ ergs; derived ages scale as $D^{5/2} (n_0/E_0)^{1/2}$. At the upper limits of our distances we find that G337.2−0.7 is less than 4500 years old and G309.2−0.6 is less than 4000 years old (the latter as previously reported by GGM). These age estimates are nicely consistent with the ejecta-dominated nature of these remnants, and furthermore any distances closer than these rough upper limits would imply correspondingly younger ages. However, since they are based on merely nominal values of the velocity, explosion energy and density, they should not be over-interpreted. Future observations with *Chandra* or *XMM-Newton* will be able to determine the blastwave temperature and emission measure (as opposed to the ejecta temperature and emission measure found here) so that we can solve for the actual E_0, n_0 and shock velocity, and directly constrain the ages of these remnants.

One would like to use the abundance ratios found in our spectral fits to determine the types of SN that formed each of these remnants. However, SNRs are spatially complex and undergo significant temporal evolution so that we do not expect all the ejecta to be at the same thermodynamic state, the reverse shock to have thermalized all the ejecta at the same time, or even for the ejecta to be uniformly distributed. In fact recent experience with *Chandra* data from Cassiopeia A (Hughes et al. 2000) has shown that for this Type II SNe, different nucleosynthetic burning products from distinct layers of the progenitor star are seen with differing thermodynamic states and at widely separate positions in the remnant. Therefore our fitted abundances, based on a single temperature, single timescale model, at best give only a rough indication of the total nucleosynthetic yields.

With the preceding caveats in mind, in Figures 5 & 8, we compare the best-fit relative abundances for G337.2−0.7 and G309.2−0.6, to nucleosynthesis models of Type Ia and II explosions from Nomoto et al. (1997), Thielemann, Nomoto, & Hashimoto (1996) and Woosley & Weaver (1995). Only the few cases that gave reasonable fits are shown. The abundance ratios for G337.2−0.7, are a decent match to the SN Ia model W7 (Nomoto et al. 1997). Type Ia produce very small quantities of low Z elements such as Ne

and Mg, and more Si-group elements such as S, Ar and Ca, which fits well with the G337.2−0.7 abundance patterns. The Fe abundance is less than that expected from the total nucleosynthetic yield, but this could simply be because the entire Fe-rich core has not yet been shocked. A low-mass SN II core-collapse model, for instance the 13 $M_{\odot}$ model of Thielemann, Nomoto, & Hashimoto (1996) (labeled TNH 13 $M_{\odot}$), is the next best fit for G337.2−0.7. The shortcoming of this model is its overprediction of the Ne and Mg abundances. However, since the low abundance of Ne and Mg is more strongly constrained than the Fe abundance, we slightly prefer the SN Ia model.

For G309.2−0.6, the case is less clear. The closest model is a 15 $M_{\odot}$ SN II model of Woosley & Weaver (1995) (labeled WW 15 $M_{\odot}$), chosen for its low Fe abundance and high S abundance. The presence of significant Ne and Mg also argues for a SN II model. However, it is clear that a global nucleosynthetic yield is an unreasonable model since there is no evidence for Fe. Determining the type of the progenitor of this remnant will require further investigation. If for instance the point source in the X-ray image of G309.2−0.6 were confirmed to be associated with the remnant and shown to be a compact remnant that would clinch its origin as a core-collapse SN.

5. Conclusions

The enhanced abundances derived from the strong X-ray emission lines of highly ionized Si, S and Ar reveal the ejecta-dominated nature of both G337.2−0.7 and G309.2−0.6. The EWs of the Si and S lines for both remnants are greater than the maximum possible EWs for solar abundance plasmas with temperatures between 0.4 and 5.0 keV. In addition the prominence of these lines compared to the Ne and Mg lines, requires non-solar abundance ratios.

Using nonequilibrium ionization thermal plasma spectral models we derive abundances for these remnants that are highly non-solar. Over the entire range in temperatures and ionization timescales, the abundances of Si, S, Ar and Ca are many times the solar values for G337.2−0.7 and for G309.2−0.6 a pure metal plasma of only Ne, Mg, Si, S and Ar (i.e., no H or He) is allowed. In addition, the elemental abundances are not well described by a single multiplicative factor times their solar abundances. For G337.2−0.7, Ne, Mg, and possibly Fe are significantly underabundant relative to the Si-group elements. For G309.2−0.6 Ne, Mg, Ar, Ca and Fe are all underabundant compared to Si and S. We thus conclude that G337.2−0.7 and G309.2−0.6 are new examples of ejecta-dominated remnants.

Furthermore our spectral fits provide us with a measure of the column densities to each remnant, which when coupled to estimates of the absorption as a function of distance along a given line of sight, provides distance estimates for both remnants. For G309.2−0.6 we find a distance of 4 ± 2 kpc consistent with both GGM's estimate from H I absorption lines, and the position of the Scutum-Crux spiral arm. For G337.2−0.7 we find an upper limit on the distance of 15 kpc, placing it no further than far side of the Norma spiral arm. Using these distances, we can place lower limits on the ages of the remnants by assuming free-expansion. G309.2−0.6 is at least 700 to 2000 years old, while G337.2−0.7 is greater than 1700 to 2600 years old. A nominal Sedov solution, $E_0 = 10^{51}$ ergs, $n_0 = 0.2$ cm^{-3} yields upper limits on the ages of 4500 years for G337.2−0.7, and 4000 years for G309.2−0.6. These age estimates corroborate our finding that both remnants are young and ejecta-dominated.

We also draw attention to the X-ray point source 1WGA J1346.5−6255, apparent within the radio shell of G309.2−0.6. We found no pulsations for this source in the 0.002 Hz to 32 Hz frequency range, but this only limits the pulsed fraction to be less than ∼85%. Although we were able to estimate its distance using the absorbing column density, we can neither exclude the possibility that it is associated with the SNR nor with the foreground open cluster NGC 5281. Higher spatial and temporal resolution observations as are possible with the *Chandra X-ray Observatory* are vital to resolve the nature of this source as well as to unambiguously distinguish between the emission from this point source and the SNR itself.

Continued investigation of ejecta-dominated SNRs such as G337.2−0.7 and G309.2−0.6 is crucial. Higher spectral resolution observations as will be possible with *XMM-Newton* and *Chandra* will allow further constraints on both the abundances and the thermodynamic state of the

shocked plasma in these remnants. Further, the breadth of possible investigations that take advantage of the 0.5″ spatial resolution of *Chandra* is staggering. Now it is possible to study the abundances of individual knots of ejecta and compare them with models of explosive nucleosynthesis from different layers in the exploding SN and thereby trace the dynamics of the explosion, as we have already begun for Cassiopeia A (Hughes et al. 2000). We can also isolate the spectrum of small-scale features in a remnant (e.g., the outermost blast-wave) and thereby study how SNe shocks impart energy to the ISM, heat electrons and ions, generate cosmic rays, and so on (see Hughes, Rakowski, & Decourchelle 2000). Thus studies of young ejecta-dominated remnants, like those presented here, with the new generation of X-ray observatories, have the potential to make a significant impact on a number of important astrophysical questions.

We thank Bryan Gaensler for use of the ATCA data on G309.2−0.6, as well as helpful commentary and Paul Plucinsky for useful discussions on the scientific content of this work. CER and JPH would like to thank Monique Arnaud for support and hospitality during the course of this work. This research has made use of the NASA Astrophysics Data System, the CDS SIMBAD database and archival X-ray data provided by the HEASARC at NASA Goddard Space Flight Center. Also shown were Digitized Sky Survey images, which were found using *SkyView* also provided by the HEASARC. Partial support was provided by NASA grant NAG5-6420.

REFERENCES

Chen, Y., Sun, M., Wang, Z., & Yin, Q. F. 1999, ApJ, 520, 737

Chevalier, R. A., & Kirshner, R. P. 1979, ApJ, 233, 154

Corbel, S., Chapuis, C., Dame, T. M., & Durouchoux, P. 1999, ApJ, 526, L29

Douvion, T., Lagage, P. O., Cesarsky, C. J. 1999, A&A, 352, L111

Fesen, R. A., Becker, R. H., & Blair, W. P. 1987, ApJ, 313, 378

Fujimoto, R., et al. 1995, PASJ, 47, L31

Green, A. J. 1974, A&AS, 18, 267

Gaensler, B. M., Green, A. J., & Manchester, R. N. 1998, MNRAS, 299, 812 (GGM)

Hamilton, A. J. S., Sarazin, C. L., & Chevalier, R. A. 1983, ApJS, 51, 115

Hughes, J. P., et al. 1995, ApJ, 444, L81

Hughes, J. P., Hayashi, I., & Koyama, K. 1998, ApJ, 505, 732

Hughes, J. P., Rakowski, C. E., Burrows, D. N., & Slane, P. O. 2000, ApJ, 528, L109

Hughes, J. P., Rakowski, C. E., & Decourchelle, A. 2000, ApJ, in press

Hughes, J. P., & Singh, K. P. 1994, ApJ, 422, 126

Hughes, J. P., Slane, P. O., & Plucinsky, P. P. 2000, ApJ, 542, in press

Leahy, D. A., Darbro, W., Elsner, R. F., Weisskopf, M. C., Sutherland, P. G., Kahn, S., & Grindlay, J. E. 1983, ApJ, 266, 160

Lucke, P. B. 1978 A&A, 64, 367

Maccacaro, T., Gioia, I. M., Wolter, A., Zamorani, G., & Stocke, J. T. 1988, ApJ, 326, 680

Moffat, A. F. J., & Vogt, N. 1973, A&AS, 10, 135

Nomoto, K., Iwamoto, K., Nakasato, N., Thielemann, F. K., Brachwitz, F., Tsujimoto, T., Kubo, Y., & Kishimoto, N. 1997, Nuclear Physics A, 621, 467

Predehl, P., & Schmitt, J. H. M. M. 1995, A&A, 293, 889

Raymond, J. C., & Smith, B. W. 1977, ApJS, 35, 419

Tanaka, Y., Inoue, H., & Holt, S. S. 1994, PASJ, 46, L37

Thielemann, F. K., Nomoto, K., & Hashimoto, M. 1996, ApJ, 460, 408

Voges et al. 1999, A&A, 349, 389

Woosley, S. E., & Weaver, T. A. 1995, ApJS, 101, 181

Yamauchi, S. 1991, ISAS Research Note 474

Whiteoak, J. B. Z, & Green, A. J. 1996, A&AS, 118, 329

This 2-column preprint was prepared with the AAS LaTeX macros v5.0.

Fig. 1.— Image of G337.2−0.7 in various bands. All grey-scales are displayed linearly from the background level to the maximum, all contours are linearly spaced from 3σ above the background to 90% of the maximum. Part a: MOST 0.8 GHz image in grey-scale, overlayed with 0.7-10.0 keV SIS contours; levels (in 10^{-3} counts s^{-1} arcminute^{-2}) 1.61, 2.24, 2.86, 3.48, 4.10. Part b: Digitized Sky Survey image overlayed with 0.7-1.5 keV SIS contours. The brightest star within the X-ray contours is HD 149901. Part c: SIS 0.7-1.5 keV; levels (in 10^{-4} counts s^{-1} arcminute^{-2}) 3.61, 4.46, 5.31,6.16, 7.01. Part d: SIS 1.5-10.0 keV; levels (in 10^{-4} counts s^{-1} arcminute^{-2}) 5.42, 13.68, 21.93, 30.19, 38.44.

Fig. 2.— Image of G309.2−0.6 in various bands. X-ray grey-scales are linearly displayed, radio and optical grey-scales use square root scaling. Part a: ATCA 1.3 GHz image with GIS broad-band (0.7-10.0 keV) contours overlayed; levels (in 10^{-4} counts s^{-1} arcminute^{-2}) 2.14, 3.46, 4.77, 6.09, 7.40. Part b: Optical Digitized Sky Survey overlayed with total *ROSAT* band contours: levels (in 10^{-3} counts s^{-1} arcminute^{-2}), 3.82, 6.57, 9.31. Part c: SIS 0.7-1.0 keV and 3.2-10.0 keV; contour levels (in 10^{-3} counts s^{-1} arcminute^{-2}) 0.559, 1.17, 1.79, 2.40, 3.02. Part d: SIS 1.0-3.2 keV; levels (in 10^{-3} counts s^{-1} arcminute^{-2}) 1.56, 2.78, 3.99, 5.20, 6.41.

Fig. 3.— The combined *ASCA* SIS0 and SIS1 spectrum of G337.2−0.7 with the best-fit varying abundance model and residuals.

Fig. 4.— χ^2 and best-fit parameter values for G337.2−0.7 as a function of kT over its 3σ allowed range. Relative abundances are relative to Si relative to solar. Indicated on the χ^2 plot are the 1, 2, and 3σ limits (dotted, dashes, dot-dashed lines respectively). For each parameter the best-fit value is indicated with an asterisk.

Fig. 5.— G337.2−0.7: The best-fit abundances of Ne, Mg, S, Ar, Ca, and Fe, relative to Si relative to solar, with 1σ errors on that ratio. Also shown are the expected relative abundances for a type Ia SNe (W7) and two type II SNe models (TNH 13 $M_\odot$ and WW 15 $M_\odot$)

Fig. 6.— The combined *ASCA* SIS0 and SIS1 spectrum of G309.2−0.6 with the nominal contamination best-fit varying abundance model and residuals. The spectrum from the hard-point source, its model and the contamination component of the SNR model (dotted curve) are also shown.

Fig. 7.— χ^2 and best-fit parameter values for G309.2−0.6 as a function of kT, for both the nominal contamination model (in bold) and the 10% less contamination model (thin lines). Abundances are relative to Si relative to solar. For each parameter, the best-fit value in the nominal contamination model is indicated with an asterisk.

Fig. 8.— G309.2−0.6: The best-fit abundances of Ne, Mg, S, Ar, Ca, and Fe, relative to Si relative to solar, with 1σ errors on that ratio, for both the nominal contamination model (solid) and the 10% less contamination model (dotted). Also shown are the expected relative abundances for a type Ia SNe (W7) and two type II SNe models (TNH 13 $M_\odot$ and WW 15 $M_\odot$)

TABLE 1
BEST-FIT PARAMETERS FOR G337.2−0.7 FOR VARYING ABUNDANCES MODEL

Parameter	Value
kT (keV)	$0.85^{+0.04}_{-0.03}$
$n_e t$ (cm^{-3} yr)	$(5.7^{+\infty}_{-3.6}) \times 10^4$
N_H (atoms cm^{-2})	$(3.5 \pm 0.3) \times 10^{22}$
Emission Integral	
$(n_e n_H V)/4\pi D^2$	$(1.7^{+0.9}_{-1.1}) \times 10^{12}$
n_H[a](atoms cm^{-3})	1.4 ± 0.3
Ne, Mg abundance[b]	$0.0^{+2.1}$
Si abundance	$5.4^{+12.2}_{-2.2}$
S abundance	$4.7^{+9.9}_{-1.8}$
Ar abundance	$2.7^{+4.6}_{-1.1}$
Ca abundance	$2.8^{+7.1}_{-2.8}$
Fe abundance	6^{+19}_{-3}
χ^2 (d.o.f.)	103.1 (67)
Reduced χ^2	1.539

[a]Derived from the emission integral with a nominal distance of 10 kpc, and the volume of a thin shell of radius 3′ as seen in the radio image

[b]Abundances relative to solar

TABLE 2
BEST-FIT PARAMETERS FOR G309.2−0.6 FOR VARYING ABUNDANCES MODEL

Parameter	Value	
	nominal contamination	10% less contamination
kT (keV)	$1.96^{+1.0}_{-0.6}$	$2.11^{+0.9}_{-1.0}$
$n_e t$ (cm^{-3} yr)	$(4.9^{+15}_{-2.0}) \times 10^3$	$(4.6^{+\infty}_{-1.7}) \times 10^3$
N_H (atoms cm^{-2})	$(0.7 \pm 0.3) \times 10^{22}$	$(0.6 \pm 0.3) \times 10^{22}$
Emission Integral		
$(n_e n_{ion} V)/4\pi D^2$	$(9.7^{+200}_{-9.7}) \times 10^8$	$(10.0^{+750}_{-10.0}) \times 10^8$
n_{ion} [a](atoms cm^{-3})	$0.02^{+0.03}_{-0.01}$	$0.02^{+0.03}_{-0.01}$
Si abundance [b]	> 34	> 11.9
Ne, Mg [c]	$0.23^{+0.09}_{-0.08}$	$0.27^{+0.19}_{-0.08}$
S [c]	$1.09^{+0.24}_{-0.18}$	$1.10^{+0.22}_{-0.17}$
Ar [c]	$0.31^{+0.21}_{-0.17}$	$0.39^{+0.21}_{-0.16}$
Ca [c]	$0.0^{+0.30}$	$0.0^{+0.45}$
Fe [c]	$0.0^{+0.03}$	$0.0^{+0.27}$
χ^2 (d.o.f.)	49.38 (53)	48.59 (53)
Reduced χ^2	0.932	0.917

[a]Derived from the emission integral with a nominal distance of 5.4 kpc, and the volume of a thin shell of radius 6′ as seen in the X-ray image

[b]Abundance relative to solar

[c]Abundances relative to Si, relative to solar, in the form: $(Z/Si) \times [(Si/H)_\odot / (Z/H)_\odot]$

SNR G337.2-0.7

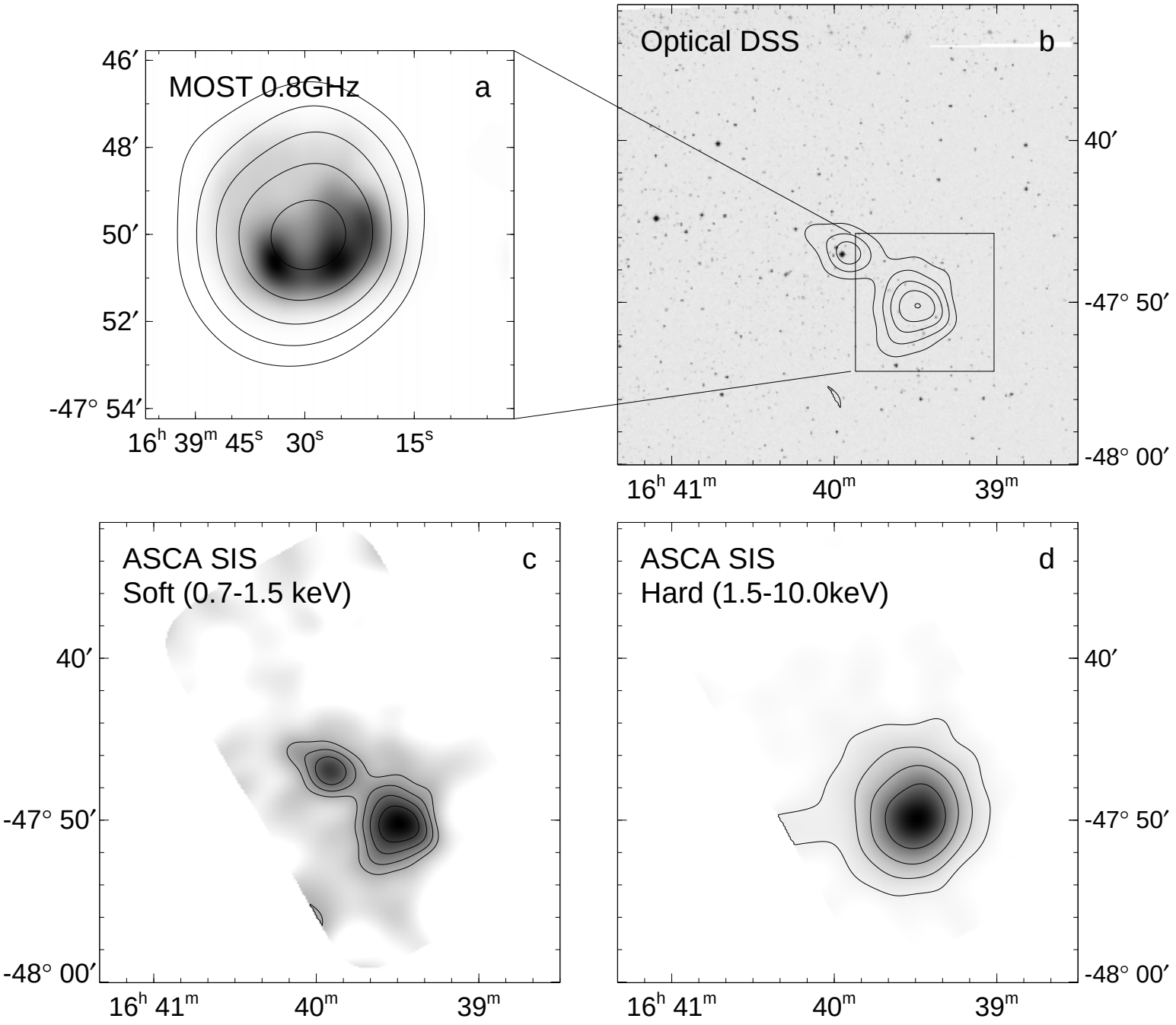
MOST 0.8GHz
a
46′
48′
50′
52′
-47° 54′
16h 39m 45s
30s
15s
Optical DSS
b
40′
-47° 50′
-48° 00′
16h 41m
40m
39m
ASCA SIS
Soft (0.7-1.5 keV)
c
40′
-47° 50′
-48° 00′
16h 41m
40m
39m
ASCA SIS
Hard (1.5-10.0keV)
d
40′
-47° 50′
-48° 00′
16h 41m
40m
39m

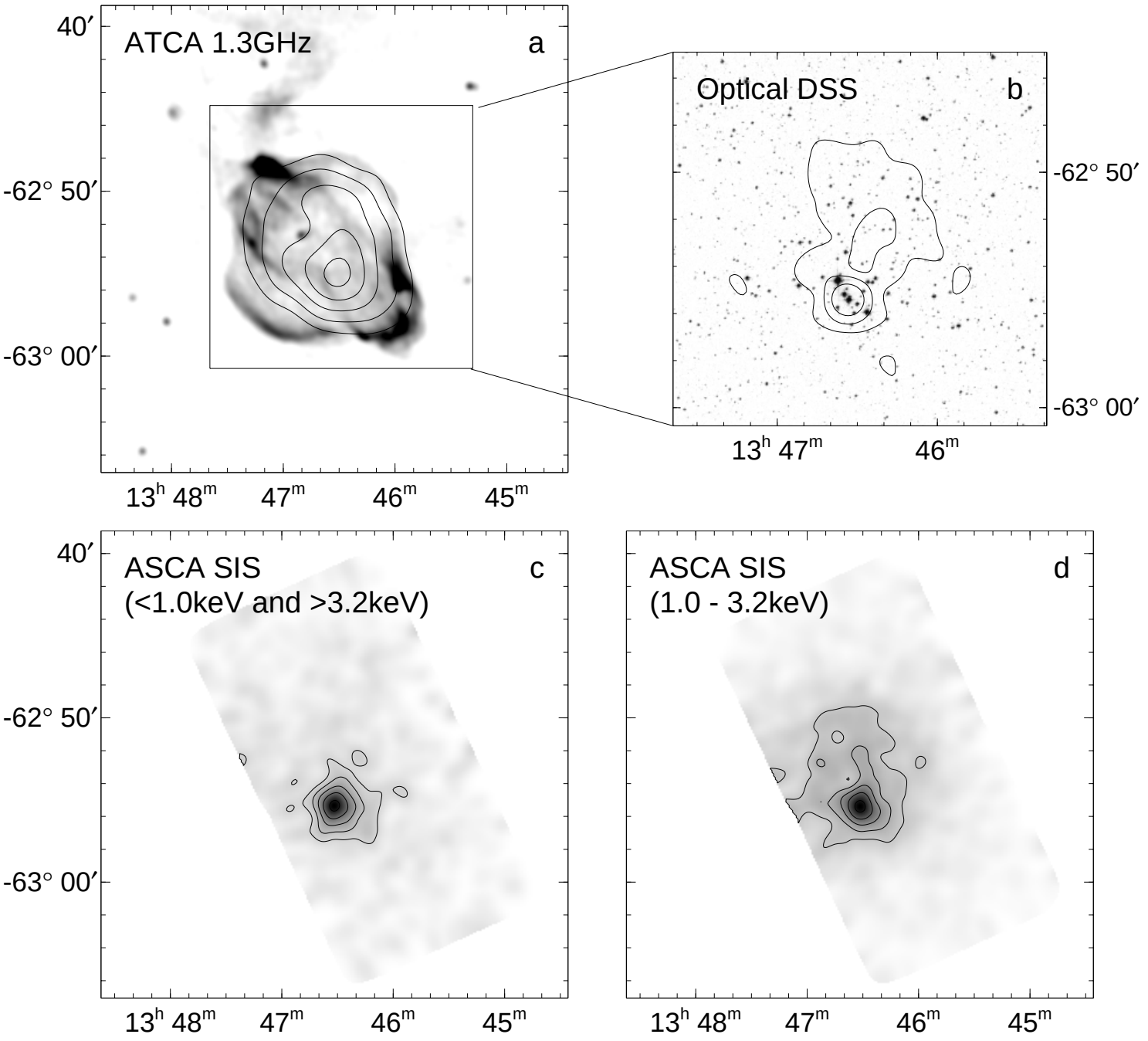
SNR G309.2-0.6
ATCA 1.3GHz
a
Optical DSS
b
c
ASCA SIS
(<1.0keV and >3.2keV)
d
ASCA SIS
(1.0 - 3.2keV)
40′
-62° 50′
-63° 00′
13h 48m
47m
46m
45m
13h 47m
46m

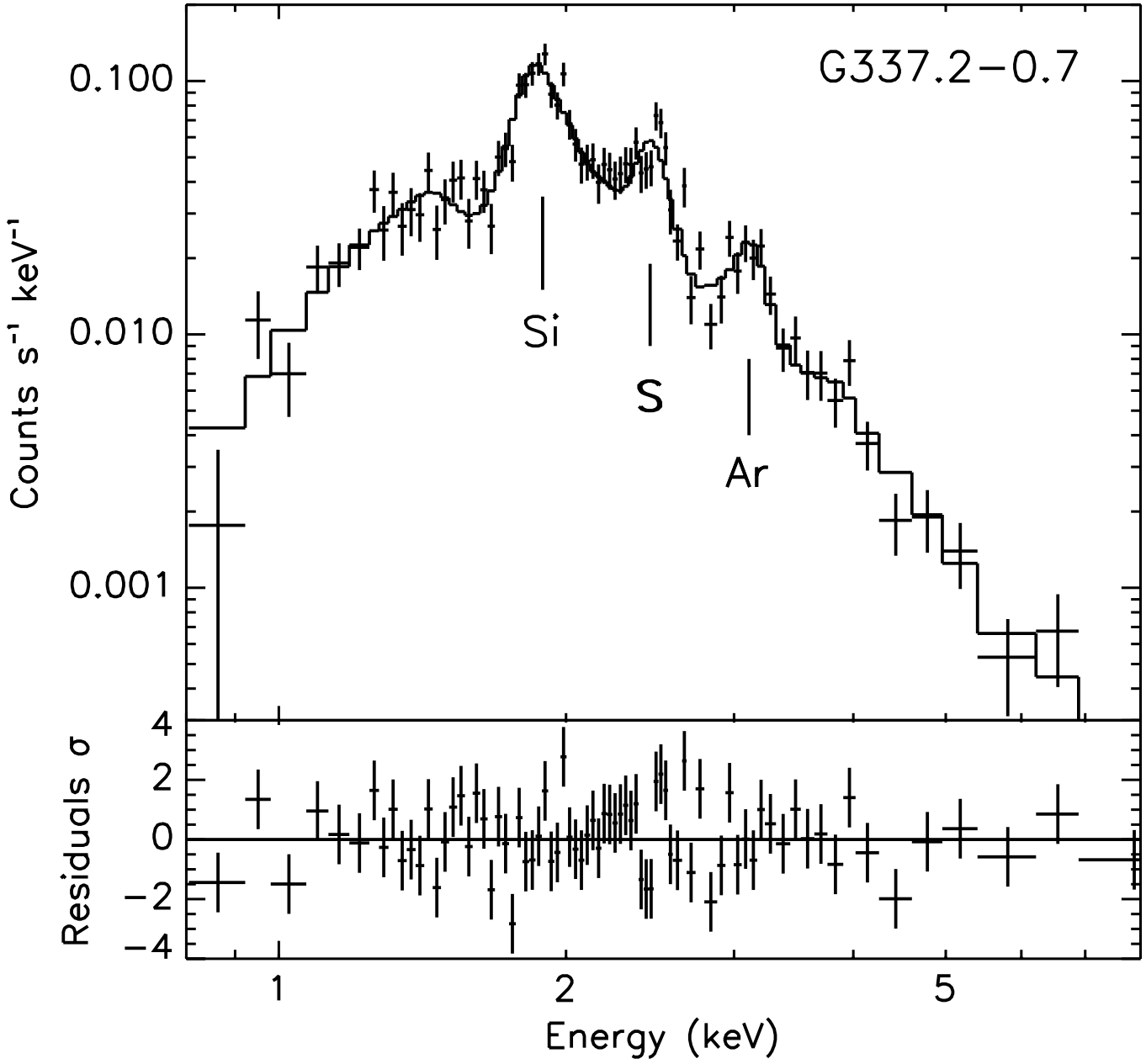
G337.2−0.7
0.100
0.010
0.001
Counts s⁻¹ keV⁻¹
Si
S
Ar
4
2
0
−2
−4
Residuals σ
1
2
5
Energy (keV)

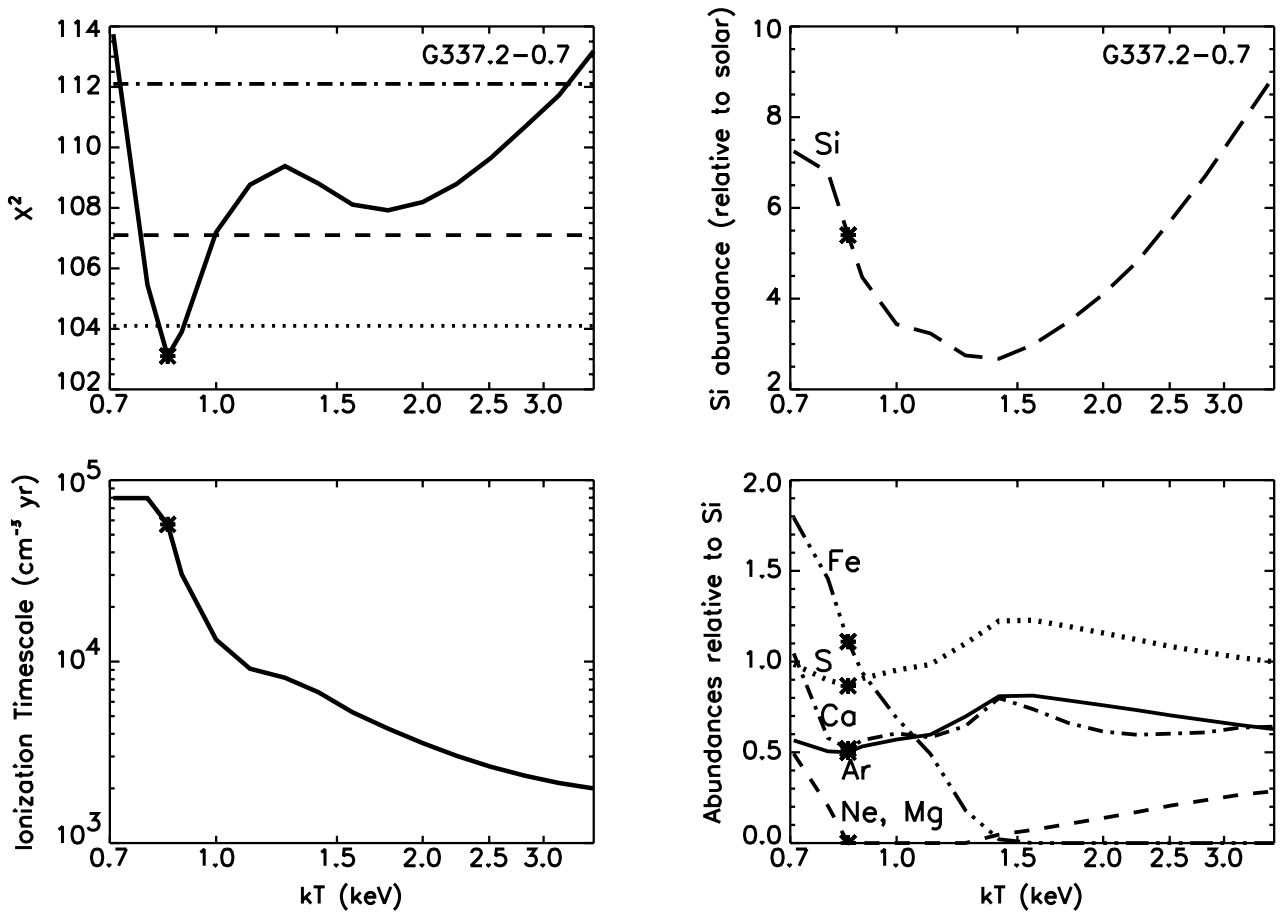
G337.2−0.7
χ²
114
112
110
108
106
104
102
0.7
1.0
1.5
2.0
2.5
3.0
G337.2−0.7
Si abundance (relative to solar)
10
8
6
4
2
Si
Ionization Timescale (cm⁻³ yr)
10⁵
10⁴
10³
kT (keV)
Abundances relative to Si
2.0
1.5
1.0
0.5
0.0
Fe
S
Ca
Ar
Ne, Mg
kT (keV)

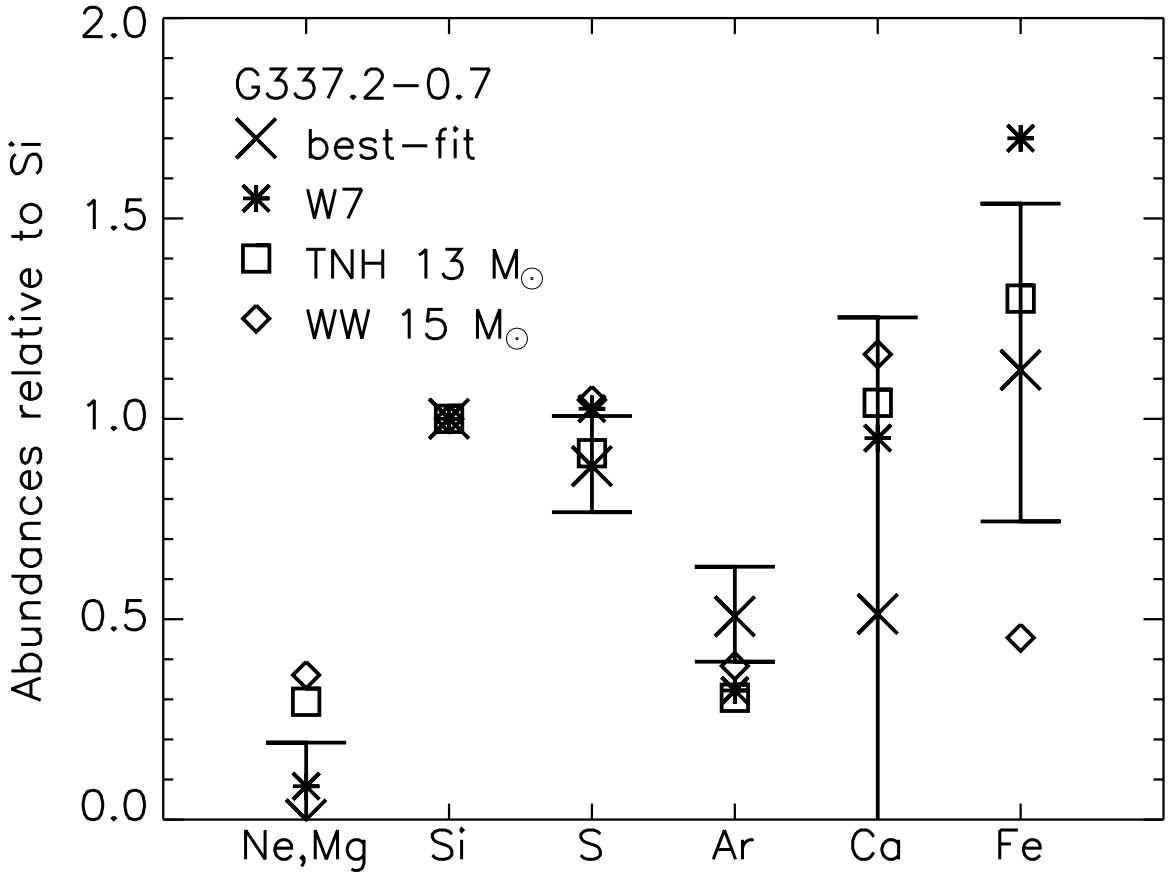
G337.2−0.7
best−fit
W7
TNH 13 M⊙
WW 15 M⊙
Abundances relative to Si
2.0
1.5
1.0
0.5
0.0
Ne,Mg
Si
S
Ar
Ca
Fe

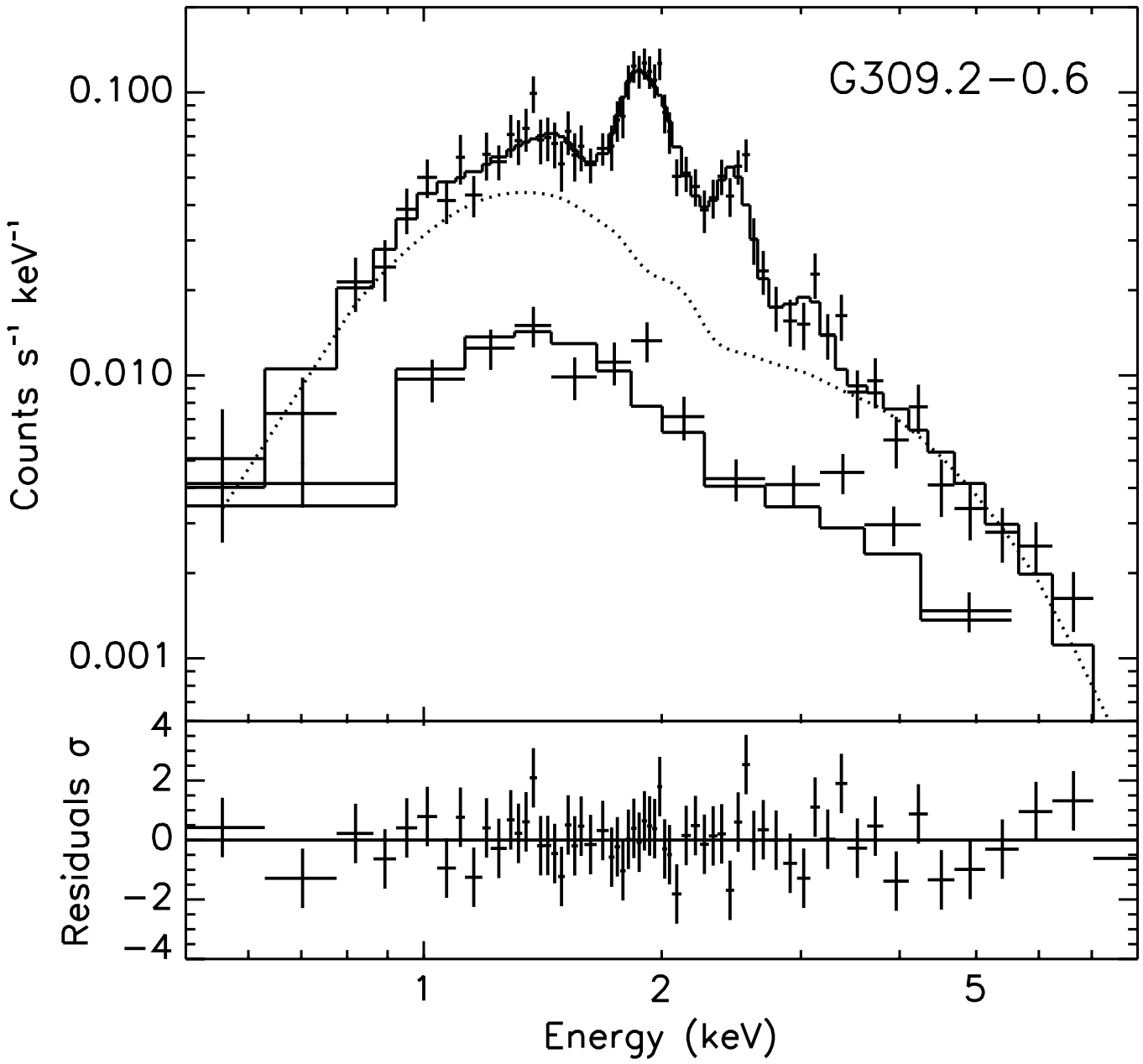
G309.2−0.6
0.100
0.010
0.001
Counts s⁻¹ keV⁻¹
4
2
0
−2
−4
Residuals σ
1
2
5
Energy (keV)

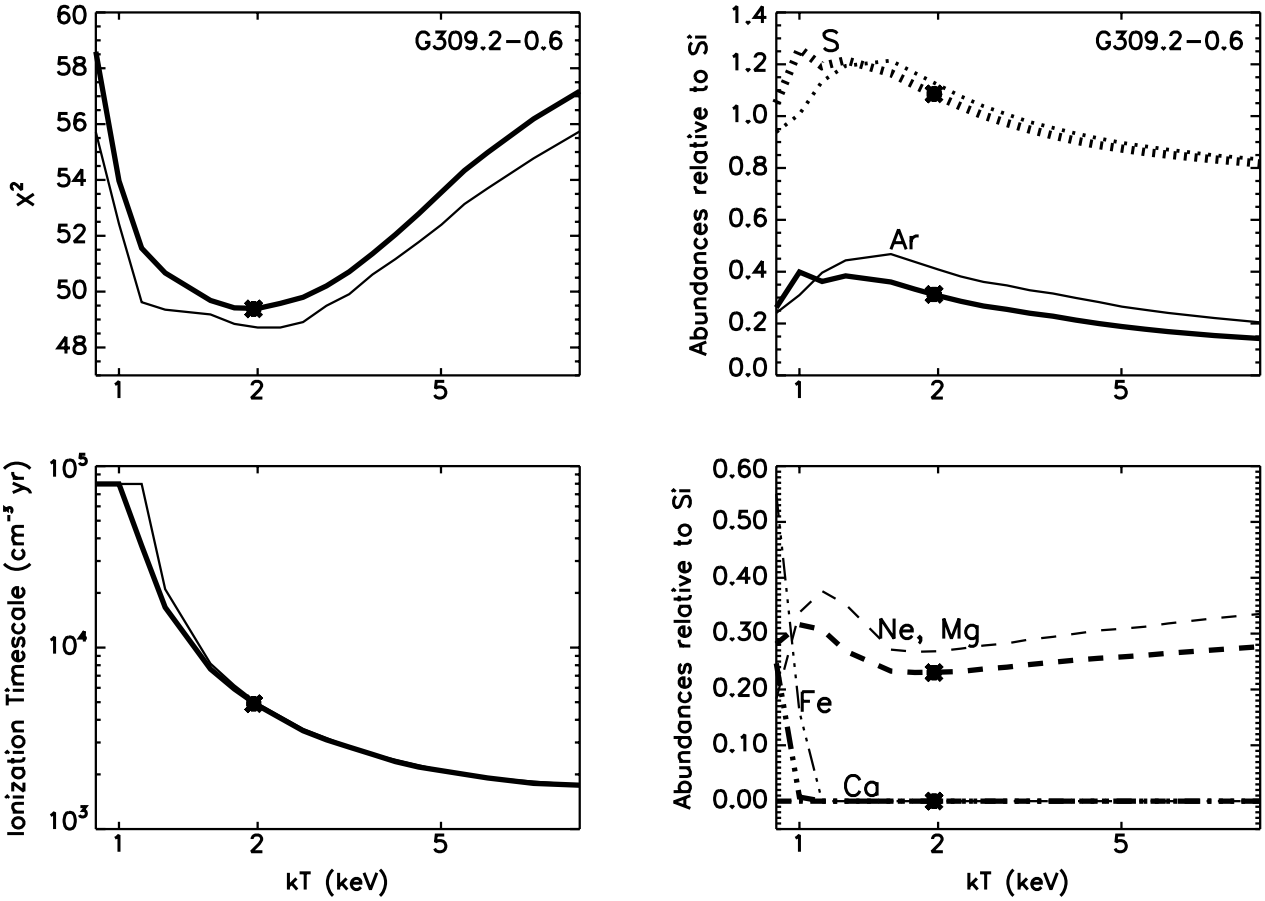
G309.2−0.6
χ²
60
58
56
54
52
50
48
1
2
5
G309.2−0.6
S
Ar
Abundances relative to Si
1.4
1.2
1.0
0.8
0.6
0.4
0.2
0.0
Ionization Timescale (cm⁻³ yr)
10⁵
10⁴
10³
kT (keV)
Ne, Mg
Fe
Ca
0.60
0.50
0.40
0.30
0.20
0.10
0.00

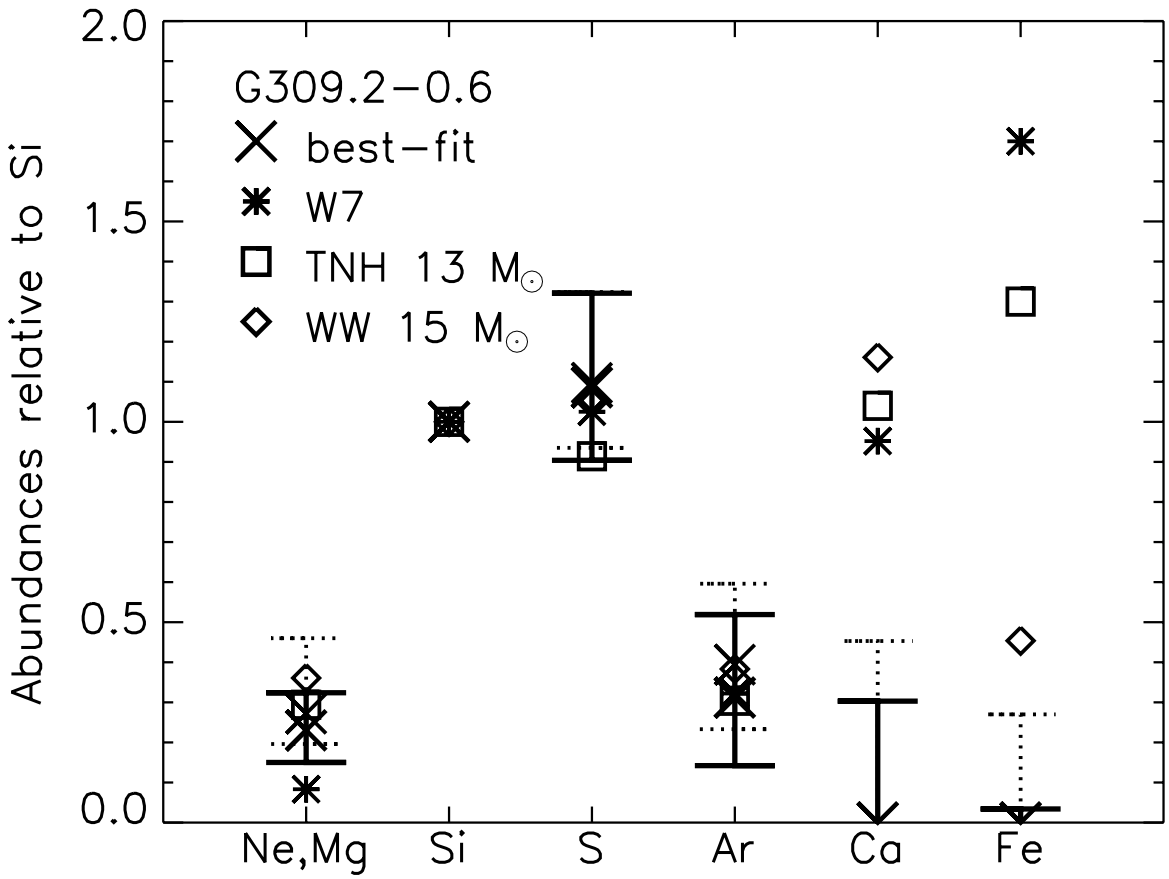
G309.2−0.6
best−fit
W7
TNH 13 M⊙
WW 15 M⊙
Abundances relative to Si
2.0
1.5
1.0
0.5
0.0
Ne,Mg
Si
S
Ar
Ca
Fe